Real-time millikelvin thermometry in a semiconductor-qubit architecture

V. Champain,[1,*] V. Schmitt,[1] B. Bertrand,[2] H. Niebojewski,[2] R. Maurand,[1] X. Jehl,[1] C.B. Winkelmann,[1] S. De Franceschi,[1] and B. Brun[1,†]

[1] *Commissariat à l'énergie atomique et aux énergies alternatives (CEA), Grenoble INP, Interdisciplinary Research Institute of Grenoble (IRIG)–Quantum Photonics, Electronics, and Engineering Laboratory (Pheliqs), Université Grenoble Alpes, Grenoble, France*

[2] *CEA Laboratoire d'électronique des technologies de l'information (Leti), Université Grenoble Alpes, Minatec Campus, Grenoble, France*

(Received 25 August 2023; revised 16 February 2024; accepted 17 May 2024; published 17 June 2024)

We report local time-resolved thermometry in a silicon-nanowire quantum dot device designed to host a linear array of spin qubits. Using two alternative measurement schemes based on rf reflectometry, we are able to probe either local electron or bosonic bath temperatures with microsecond time scale resolution and a noise-equivalent temperature of 3 $\mathrm{mK}/\sqrt{\mathrm{Hz}}$. Following the application of short microwave pulses, causing local periodic heating, time-dependent thermometry can track the dynamics of thermal excitation and relaxation, revealing clearly different characteristic time scales. This work opens important prospects to investigate the out-of-equilibrium thermal properties of semiconductor quantum electronic devices operating at very low temperature. In particular, it may provide a powerful handle to understand heating effects recently observed in semiconductor spin-qubit systems.

DOI: 10.1103/PhysRevApplied.21.064039

I. INTRODUCTION

Quantum electronics embraces a large variety of devices the functionality of which relies on quantum mechanical properties such as size quantization, phase coherence, entanglement, etc. Cryogenic operation is generally required for the emergence of such properties and, at low temperature, the time scales for energy exchange and thermalization processes tend to increase dramatically, leading to metastable regimes and to the coexistence of thermal (and nonthermal) baths that are strongly out of equilibrium. The understanding and control of these thermodynamical aspects is not only mandatory for the development and operation of bolometers, cryogenic thermometers or coolers; it can also be particularly crucial for improving the performance and scalability of solid-state devices for quantum sensing and quantum computing. To this aim, access to thermometers capable of measuring local temperatures faster than the characteristic time scales of heat exchange dynamics is of primary importance [1].

In this work, we address this point in the context of semiconductor quantum dot (QD) devices, largely motivated by their prospects for scalable spin-based quantum computing. The operation of semiconductor spin qubits requires the application of high-frequency signals that unavoidably dissipate energy into the qubit environment due to the Joule effect and dielectric losses. This raises severe practical issues regarding spin-qubit addressability, since a significant temperature dependence of their Larmor frequencies has recently been reported [2]. Fast temperature changes due to unintentional heating can lead to spin decay and dephasing [3,4], thereby reducing gate and readout fidelities [5]. This problem worsens for increasing numbers of qubits and corresponding control gates, leading to a clear bottleneck for large-scale integration. A higher operation temperature can mitigate the impact of local heating [2] but at the price of a reduced spin coherence time [6,7]. Therefore, understanding the modality and dynamics of heating from microwave excitation is a necessary step to devise more efficient measures to preserve qubit performance. To this end, access to fast time-domain thermometry compatible with millikelvin temperature and hundreds of millitesla fields can be a clear asset.

The most advanced local thermometry techniques in quantum circuits rely on metal-superconductor junctions [8–10]. These thermometers are incompatible with spin-based quantum processors, due to integration constrains and to their susceptibility to magnetic fields. Semiconductor QD thermometers [10–14], on the other hand, do not suffer from these limitations. Moreover, they can measure the temperature of an electronic reservoir without requiring galvanic coupling [14–16].

*Corresponding author: victor.champain@cea.fr
†Corresponding author: boris.brun-barriere@cea.fr

Here, we apply this approach to silicon QD devices. By adjusting the tunnel coupling between the QD thermometer and a probed electronic reservoir, we are able to preserve its sensitivity down to the base temperature (55 mK) of a dilution refrigerator. In addition, by adopting an isolated double-dot configuration of the QD thermometer, we extend our thermometry capabilities to probe the local bosonic temperature. We simultaneously show that this thermometer can perform time-domain measurements at the microsecond scale.

II. DEVICE AND OPERATION MODES

The QD devices consist of silicon-on-insulator metal-oxide-semiconductor (MOS) nanowires with a rectangular cross section of 80×16 nm^2. The nanowires are covered by a set of eight parallel gates with a pitch of 80 nm [see the example in Fig. 1(a)]. Due to p-doped leads, holes are accumulated under negatively biased gates as schematically shown in Fig. 1(b).

We investigate two different device settings. In the first setting (I), we define a single QD tunnel coupled to the hole reservoir in one of the two degenerately doped contact leads, as shown on the left-hand side of Fig. 1(b). The impedance of a lumped-element LC circuit connected to the same lead is sensitive to charge tunneling between the QD and the lead. Both dissipative and capacitive changes can be detected through reflectometry measurements [18–20].

The second setting (II) requires biasing four consecutive gates, as shown on the right-hand side of Fig. 1(b). The two inner gates (G6 and G7) define a double QD, whereas the outer ones (G5 and G8) allow full isolation of this double QD from the remaining part of the channel and from the leads [21,22]. Readout is now performed by reflectometry on an inner gate electrode (G7), with interdot tunneling resulting in a quantum capacitance contribution [18,19,23].

The tank circuits used for rf reflectometry are formed by classical surface-mount inductors and parasitic capacitances. While different values of inductance have been used, all resonances are around 400 MHz, with few-to-several megahertz bandwidth (for details, see the Supplemental Material [17]). The reflectometry measurements are performed in a weak-coupling dispersive regime, in which the phase shift of the reflected signal is directly proportional to the frequency shift and thus to the quantum capacitance [18,23–25].

III. QUANTUM-DOT THERMOMETRY: BASIC PRINCIPLES AND EXPERIMENTAL IMPLEMENTATION

In both experimental configurations, the quantum capacitance contribution is expected to depend on temperature. In setting I, where a single level is tunnel coupled to a

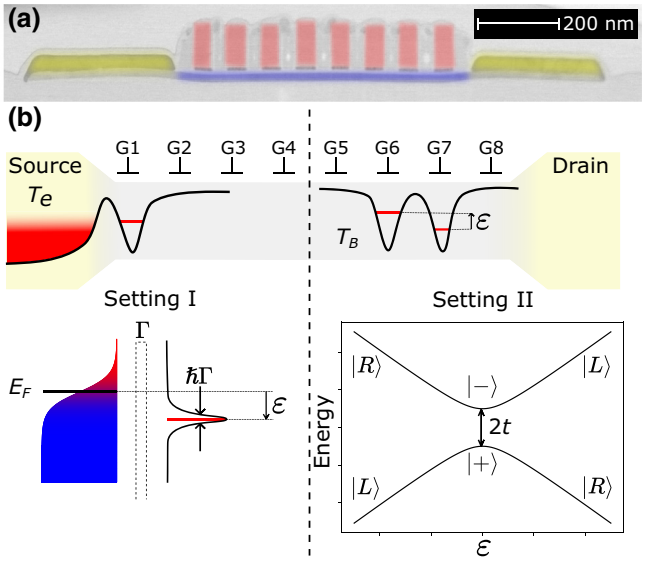

FIG. 1. The device and charge configuration for two thermometry techniques. (a) A false-color tunneling electron micrograph of a representative MOS device with a silicon-nanowire channel (blue), highly doped conductive leads (yellow), and eight parallel gates (red). Note that the gates can be considered metallic; however, the contacts on the leads and gates are made of tungsten vias, which are superconducting at base temperature. Three different samples have been measured in this work (for details, see the Supplemental Material [17]). (b) A schematic of an eight-gate device, illustrating the two thermometry methods. The source and drain (yellow) are highly p doped to form metallic leads acting as hole reservoirs. Quantum dots (QDs) can be defined along the undoped silicon channel (blue) by means of gates G1–G8. In the first type of thermometer (setting I), G1 defines a single QD tunnel coupled to the source reservoir as illustrated by the hole-energy diagram just below. The hole reservoir is modeled by a Fermi distribution with electronic temperature T_e, while the dot is modeled by a single level the line width of which is determined by the tunnel rate Γ. The detuning, ε, is defined here as the difference between the QD electrochemical potential and the Fermi level in the reservoir. In the second thermometer (setting II), a double QD isolated from the reservoirs is defined under G6 and G7. Both QDs are modeled by single levels with a tunnel coupling t and detuning ε. The corresponding energy diagram is shown just below, with $|L\rangle$ ($|R\rangle$) representing the state localized in the left (right) QD at large detuning, and $|+\rangle$ ($|-\rangle$) the hybridized bonding (antibonding) state at zero detuning. The coupling to the leads is completely suppressed by means of the two side gates G5 and G8.

Fermi sea, the quantum capacitance reads [11,14,16]

$$C_q(\varepsilon) = \alpha^2 e^2 \int_{-\infty}^{+\infty} \left(\frac{1}{4k_B T_e} \cosh\left(\frac{e\alpha\varepsilon - E}{2k_B T_e} \right)^{-2} \right) \times \left(\frac{\hbar\Gamma}{\hbar^2\Gamma^2 + E^2} \right) \mathrm{d}E \qquad (1)$$

(for details, see the Supplemental Material [17]). Here, e is the electron charge, k_B the Boltzmann constant, $\hbar$ is the reduced Planck constant, α is the gate lever-arm parameter, ε is the detuning (in gate voltage), and Γ is the dot-lead tunnel rate. The relevant temperature is the electronic temperature of the lead, T_e. The quantum capacitance is therefore a convolution of two peaks: the derivative of the Fermi distribution, broadened by $k_B T_e$, and the dot density of states, modeled by a Lorentzian of width $\hbar\Gamma$. Thermal broadening dominates for $\hbar\Gamma < k_B T_e$.

In setting II, hybridization of the orbitals in the left and right QDs results in a two-level system in the canonical ensemble. The corresponding energy diagram as a function of the gate-dependent level detuning, ε, is characterized by an avoided level crossing due to the interdot tunnel coupling t. The quantum capacitances associated with the bonding and antibonding states have opposite signs, since they are directly related to the curvatures of the corresponding energy-versus-detuning relations [25]. The total capacitance is given by the sum of the two quantum capacitances weighted by the population of the bonding and antibonding states, $P_{|+\rangle}$ and $P_{|-\rangle}$ (for details, see the Supplemental Material [17]), i.e. [11,25,26],

$$C_q(\varepsilon) = \alpha^2 e^2 \frac{2t^2}{\left((\alpha e\varepsilon)^2 + 4t^2\right)^{3/2}} \tanh\left(\frac{\left((\alpha e\varepsilon)^2 + 4t^2\right)^{1/2}}{2k_B T_B}\right), \tag{2}$$

where T_B stands for the Boltzmann temperature of the double dot, given by the relative population in both states, $k_B T_B = 2t/\ln(P_{|+\rangle}/P_{|-\rangle})$. At thermal equilibrium with the thermal bath, i.e., in the absence of external charge drive, the Boltzmann temperature equals the bath temperature. We note that $C_q(\varepsilon)$ is peaked at $\varepsilon = 0$, with a line width solely determined by the tunnel coupling t and an amplitude that becomes strongly temperature dependent in the limit $t \lesssim k_B T_B$.

Both settings are experimentally tested by thermally anchoring the device to the mixing chamber of a dilution refrigerator with a base temperature of 55 mK and the results are shown in Fig. 2. We initially verify that the impedance of the LC resonator itself is temperature independent in the range of interest. In Fig. 2(a), we present the temperature dependence of the reflected signal measured in the case of setting I [left-hand side of Fig. 1(b)]. The data are obtained after selecting the dot-lead transition with the narrowest Coulomb peak resonance (for details, see the Supplemental Material [17]). The phase of the reflected signal displays a peak proportional to the expected peak in $C_q(\varepsilon)$, the amplitude of which decreases with the mixing-chamber temperature, T_{MC}, while its width increases. This is in very good agreement with Eq. (1), which we use to fit the experimental peaks (for details, see the Supplemental Material [17]). We find a tunnel coupling $\Gamma/2\pi = 383 \pm 38$ MHz, an order of magnitude lower than $k_B T_e/h$ at base temperature, thereby fulfilling the condition for proper temperature sensitivity.

For the case of setting II [right-hand side of Fig. 1(b)], we first load a few holes under G6 and G7 by applying negative voltages to G6, G7, and G8. Bringing G8 back to zero voltage results in the trapping a few charges confined to a double QD controlled by G6 and G7. Provided that the interdot tunnel coupling is greater than the LC resonator frequency, charge transitions from one dot to the other can be detected by rf reflectometry. In this isolated regime, dot-lead transitions are inhibited and the interdot transitions are the only visible spectroscopic features, extending over the entire stability diagram [21,22] (for details, see the Supplemental Material [17]). As we follow the interdot transition toward more negative voltages, we create deeper electrostatic quantum wells, effectively increasing the barrier height and hence lowering t. We can thus achieve a regime where the thermal population of the double-QD two-level system becomes highly sensitive to the bath temperature T_B. Similarly to the first configuration, we measure the interdot transitions as a function of T_{MC}, the results being shown in Fig. 2(b). Fitting to Eq. (2) yields a tunnel rate $t/h = 2.03 \pm 0.04$ GHz. Even though the gap due to level repulsion is 4 times larger than the thermal energy at base temperature, we still have a 2% thermal occupation of the excited state. This ensures a measurable temperature dependence of the quantum capacitance all over the explored temperature range. Yet extending this measurement technique to even lower temperatures would require reducing the tunnel coupling accordingly, as discussed later. Nonetheless, we note that the relatively low tunnel coupling achieved here enables us to operate this nongalvanic thermometer at temperatures an order of magnitude lower than previously reported [16].

The measured temperatures extracted from the fits are shown in Figs. 2(c) and 2(d) as a function of T_{MC} in setting I and II, respectively. At relatively high temperature, both T_e and T_B follow the mixing-chamber temperature closely, except for significant deviations above 500 mK that can be attributed to the population of higher-energy QD levels, which is not taken into account in our models.

Below about 100 mK, however, the two experimental settings exhibit different behaviors. In setting I, the measured electronic temperature saturates. This trend, commonly observed in cryogenic experiments, is due to the residual electromagnetic noise coming from the circuitry at higher temperature, combined with the vanishing thermal coupling of electrons to their environment [27,28]. The inset in Fig. 2(c) shows a close-up of these data points, with a fit to a saturation function $T_e = (T_{\mathrm{MC}}^n + T_0^n)^{1/n}$, here yielding $n = 3.4$ and a saturation temperature $T_0 = 84$ mK. In the case of an electron-phonon-dominated thermalization [10], one would expect $n = 5$ in degenerately doped silicon [27]. However, the structure of the lead in our

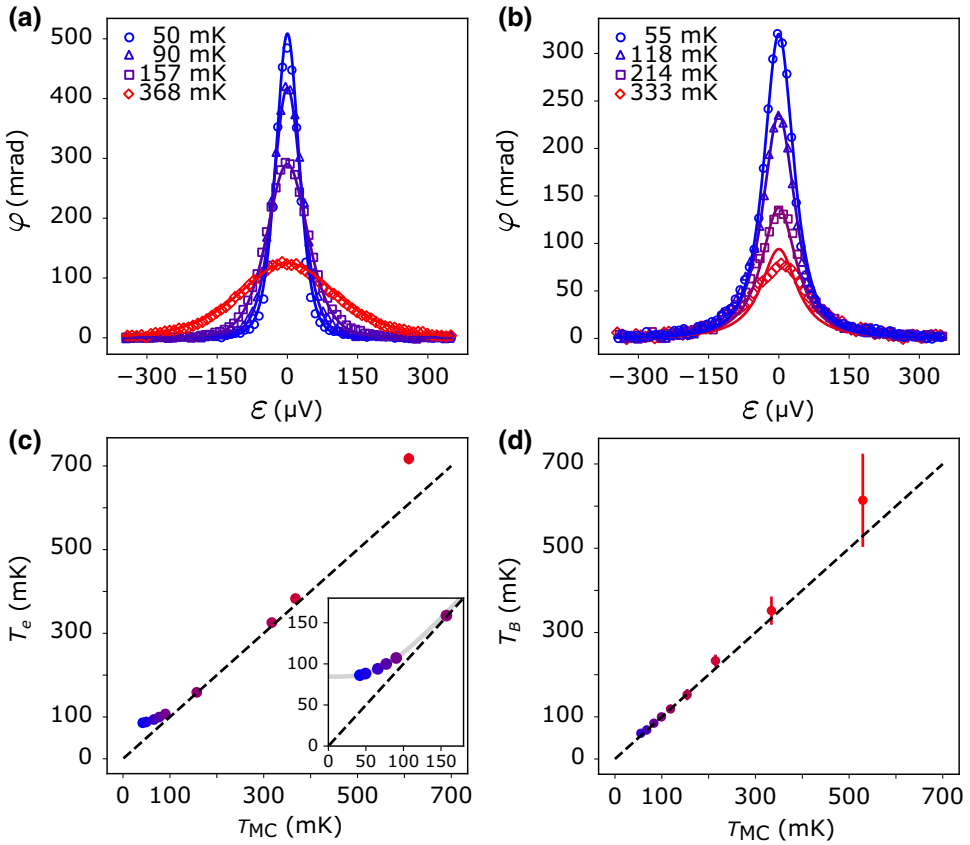

FIG. 2. An experimental demonstration of the two thermometry techniques. (a) Setting I: the phase of the reflectometry signal from the tank circuit as a function of the detuning, for a dot-lead transition at different mixing-chamber (MC) temperatures. The peak amplitude is decreasing with temperature while the peak width increases. (b) Setting II: the phase of the reflectometry signal for an interdot transition as a function of the MC temperature. The peak amplitude is decreasing, while the width remains unchanged. (c) The T_{MC} dependence of the electronic temperature, T_e, in the source reservoir as obtained from fitting to Eq. (1). The inset shows a close-up of the low-temperature saturation. (d) The T_{MC} dependence of T_B, as obtained from fitting Eq. (2)).

experiment also involves other materials in close vicinity, including metallic and/or superconducting vias, hindering an accurate thermal modeling.

Interestingly, no such saturation is observed in the case of setting II. Indeed, here the isolated double-QD is not coupled to any Fermi sea and its temperature is determined by the interaction with the local bosonic baths, i.e., lattice phonons and photons in the electromagnetic environment.

IV. THERMOMETER CALIBRATION AND OPTIMIZATION

We now investigate the possibility of performing local thermometry in the time domain. We focus on setting II. The peak amplitude of the phase shift at zero detuning strongly depends on the bath temperature and it can be measured on a microsecond time scale. This opens up the possibility of monitoring the time evolution of T_B, provided that thermal equilibration between the QD two-level system and the surrounding bath occurs on a shorter time scale.

To precisely calibrate this thermometer, we measure the reflected signal phase at zero detuning, φ_0, and vary the mixing-chamber temperature. The resulting calibration curve is shown in Fig. 3(a). From Eq. (2), by taking $\varepsilon = 0$ and, based on Fig. 2(d), $T_B = T_{\mathrm{MC}}$, we obtain

$$\varphi_0 = \kappa \times \frac{1}{2t} \tanh\left(\frac{t}{k_B T_{\mathrm{MC}}}\right), \tag{3}$$

where κ is a proportionality coefficient that does not depend on temperature.

The data are in good agreement with this model [solid red line in Fig. 3(a)], where t and κ are the free parameters. We note that, in principle, the anticrossing gap ($2t$) in such a configuration could be independently measured through Landau-Zener-Stückelberg interference [29,30]. Such an additional measurement would make this type of thermometer a primary one, removing the need for a calibration process.

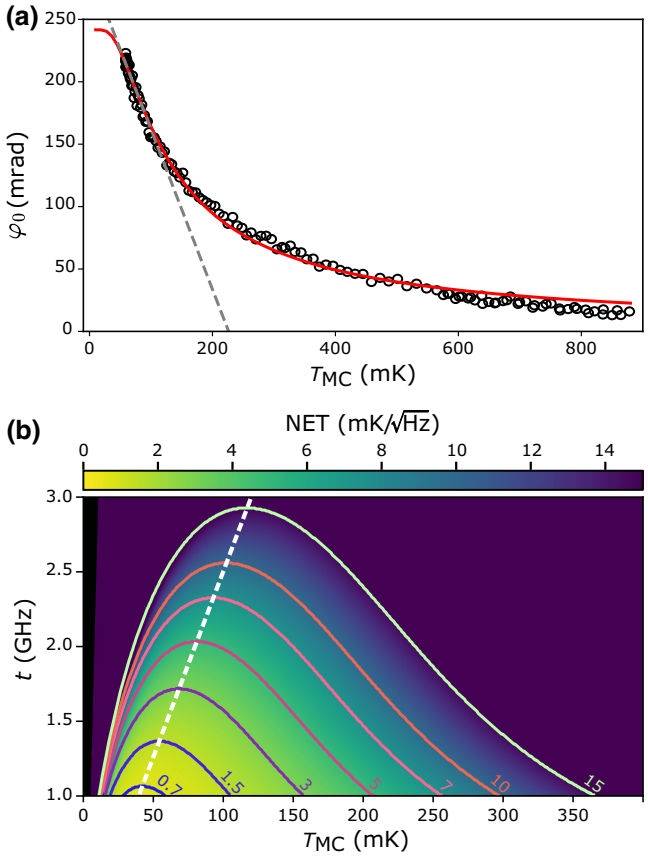

FIG. 3. The thermometer calibration and optimal operation regime for setting II. (a) The peak amplitude, φ_0, as a function of T_{MC} in the case of setting II. The experimental data (open circles) are fitted to Eq. (3) (solid red line), giving a tunnel rate $t/h = 1.72 \pm 0.04$ GHz. The dashed gray line is a linear fit to the data in the 55–100 range of highest sensitivity ($|\partial\varphi_0/\partial T| = 1.28$ mrad/mK). (b) The calculated noise-equivalent temperature, NET, versus (T_{MC},t). Iso-NET curves are drawn in blue and yellow colors. The dashed white line highlights the t dependence of the NET minimum (i.e., the T_{MC} at which $\partial \mathrm{NET}/\partial T_{MC} = 0$).

Notably, the model used for the fit in Fig. 3(a) predicts a saturation of the peak amplitude at low temperature, i.e., when the population of the antibonding state becomes negligibly small ($\lesssim 0.5\%$). In our experimental conditions, this saturation is not observed because it occurs slightly below the mixing-chamber base temperature. In Fig. 3(a), we also show that the thermometer sensitivity (proportional to $|\partial\varphi_0/\partial T_{MC}|$) becomes maximal close to the fridge base temperature, i.e., just above the expected low-temperature saturation. The dashed gray line in Fig. 3(a) is a linear fit around the point of maximal sensitivity (55–100 mK).

To further characterize the thermometer performance and deepen our understanding of its optimal operating conditions, we now turn to the evaluation of the noise-equivalent temperature (NET) and its dependence on t and T_{MC}. Since $\mathrm{NET} = (S_{\varphi\varphi}/|\partial\varphi_0/\partial T_{MC}|)$, where $S_{\varphi\varphi}$ is the phase-noise amplitude, we begin by recording the phase signal at various sampling rates, covering a large frequency domain. The measured spectrum reveals a white-noise floor at $S_{\varphi\varphi} = 3.9 \pm 0.2$ mrad/$\sqrt{\mathrm{Hz}}$, which is consistent with the expected noise from the first amplification stage at 4 K. This gives $\mathrm{NET} = 3.0 \pm 0.2$ mK/$\sqrt{\mathrm{Hz}}$ in the maximal sensitivity low-temperature region of Fig. 3(a). This value is expected to change by varying the interdot tunnel coupling and the temperature range of operation. To fully capture this dependence, implicitly coming from the $|\partial\varphi_0/\partial T_{MC}|$ term, we make use of Eq. (3), with the additional hypothesis of a dispersive coupling between the LC resonator and the isolated double QD, which implies [24]

$$\kappa = A_0 \left(\frac{1}{2t + f_r} + \frac{1}{2t - f_r} \right), \tag{4}$$

where f_r is the resonant frequency of the tank circuit and A_0 is a constant depending only on circuit parameters, the value of which can be deduced from the fit of Fig. 3(a). The resulting $\mathrm{NET}(T_{MC}, t)$ map, extrapolated from the data in Fig. 3(a), is shown in Fig. 3(b).

For a given tunnel coupling, the thermometer is expected to have an optimal temperature at which the NET is minimized. The dashed white line highlights the t dependence of this optimal operation temperature. Interestingly, reducing the tunnel coupling at fixed temperature always results in a lower NET no matter what the temperature is. Therefore, operating at weak tunnel coupling is generically beneficial. However, this only holds as long as the dynamics of the LC resonator are slow with respect to interdot tunneling (adiabatic limit), i.e., away from the divergence in Eq. (4) for $t \sim 2f_r$. For this reason, the calculation in Fig. 3(b) is limited to $t \geq 1$ GHz. (Below this cutoff, other physical mechanisms such as charge noise would also limit the thermometer sensitivity.) For $t = 1$ GHz, the thermometer NET could be as low as 1 mK/$\sqrt{\mathrm{Hz}}$ at 30 mK. Moreover, a better impedance matching between the device and the LC resonator would result in a larger A_0 and hence an even lower NET, thereby approaching and possibly exceeding the performance of state-of-the-art metal-superconductor thermometers [8].

V. PROOF OF CONCEPT: REAL-TIME THERMOMETRY

Finally, we address the use of our device for real-time thermometry. The measured NET is in principle too large to allow stochastic temperature fluctuations to be resolved at a microsecond time scale. However, the developed thermometry could still be applied to probe the dynamics of local thermal exchange caused by deterministic and periodic heating events, such as those associated with the sequences of microwave bursts typically employed in the

operation of spin-qubit devices. Under these conditions, the signal-to-noise ratio can be increased by averaging over multiple cycles. As a result, the thermometry bandwidth is no longer limited by the NET but by the response time of the system itself.

We identify two fundamentally limiting bandwidths. The first is the response time of the measurement apparatus. It would be defined here by the bandwidth of the resonator, allowing for a time resolution of approximately 20 ns (7.8 MHz). The second limiting factor is the charge relaxation time $T1$ toward a thermal state, since the measurement of the Boltzmann temperature is only meaningful at thermal equilibrium. This happens in this system in about 15 ns (for details, see the Supplemental Material [17]), whereas maximal relaxation times of about 100 ns have been reported in similar devices [31]. Double quantum dot (DQD) thermometry is therefore robust up to a few megahertz.

For a proof-of-concept demonstration of time-resolved thermometry, we periodically induce local heating by means of microwave bursts applied to a nearby gate, other than the gates defining the double-dot thermometer. The data acquisition is synchronized with the applied bursts to monitor the locally induced temperature modulation [8].

We plot the resulting phase signals versus time in Fig. 4. We observe the system switching between two phase levels, φ_{on} if the microwave is on and φ_c when it is off. These values would translate to 75 mK and 55 mK, respectively,

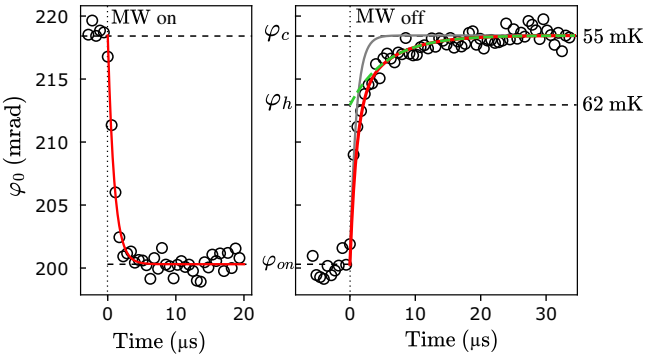

FIG. 4. Real-time thermometry with setting II. Microwave bursts are periodically applied to gate G5, adjacent to the double-dot thermometer. The microwave of frequency 15 GHz and power −40 dBm is modulated by a square signal of frequency 20 kHz, resulting in 50-μs-long bursts, with 50-μs waiting time between each burst. The phase signal is acquired with a synchronized lock-in at a sampling rate of 1.7 MHz, with a 400-ns integration time. It is averaged over 2×10^6 cycles and is plotted as a function of time (open circles). (a) Heating: at each cycle, the microwave burst is turned on at Time = 0 and the phase φ_0 decreases from $\varphi_c \sim 220$ to $\varphi_{\text{on}} \sim 200$ mrad. (b) Cooling: the microwave excitation is switched off at Time = 0 and the phase increases back to φ_{on} with a two-stage relaxation (for details, see the text).

with the previous calibration. However when the drive is on, nonadiabatic (Landau-Zener) processes can occur and populate the excited state of the double dot. This would decrease the phase measured. The bath temperature of the "warm" stage can then hardly be precisely known. After the drive is turned off, the phase increases back to thermal equilibrium.

However, the transient regimes exhibit different characteristic time scales for cooling and heating. We model the time evolution after the microwave is turned on by an exponential decay,

$$\varphi_0(\tau) = \varphi_{\text{on}} + (\varphi_c - \varphi_{\text{on}}) \exp(-\tau/\tau_m), \tag{5}$$

which we plot as solid red lines in Fig. 4. We find a characteristic time $\tau_m = 0.93 \pm 0.35$ μs close to our experimental time resolution, which is set by the lock-in measurement bandwidth.

The cooling dynamics reveal two relaxation processes, as evidenced in Fig. 4(b). The first relaxation corresponds to the rapid thermalization of the QD thermometer. This occurs on the characteristic time scale for charge relaxation, $T1$, which we estimate to be about 15 ns (for details, see the Supplemental Material [17]). Since $T1 \ll \tau_m$, these charge-relaxation dynamics cannot be resolved and the phase decay is again limited by the measurement bandwidth. A single relaxation on time scale τ_m, however, cannot capture the whole dynamics, as evidenced by the comparison to the gray line in Fig. 4. A second slower relaxation, with a characteristic decay time of $\tau_b = 6.0 \pm 1.5$ μs, is in fact observed. We ascribe this to the relaxation of the heat bath, which can be revealed once the QD thermometer has thermalized with the surrounding bath. We then propose a more complete model, including a relaxation of the thermometer toward equilibrium with the bath at time τ_m,

$$\varphi_0(\tau) = \varphi_{\text{bath}}(\tau) + (\varphi_{\text{on}} - \varphi_{\text{bath}}(\tau)) \exp(-\tau/\tau_m), \tag{6}$$

while the bath relaxes at time τ_b:

$$\varphi_{\text{bath}}(\tau) = \varphi_c + (\varphi_h - \varphi_c) \exp(-\tau/\tau_b). \tag{7}$$

Substitution of Eq. (7) into Eq. (6) leads to the red model in Fig. 4(b), while φ_{bath} is plotted with a dashed green line. We can extrapolate the relaxation of the bath at *Time* = 0 to estimate a bath temperature of approximately 62 mK in the presence of heating, effectively smaller than 75 mK.

A deeper investigation (e.g., to explore the effect of varying the microwave excitation cycles and the way in which they are applied) could provide important missing information about the dissipation mechanisms and the nature of the thermal bath in the QD environment.

Previous works on different types of Si-based spin-qubit devices have indirectly inferred thermal relaxation times

from time-resolved Larmor frequency shifts attributed to local overheating [2,4,32]. As compared to this recent literature, the relaxation times reported here are either comparable [4] or significantly shorter [2,32]. The discrepancy could be ascribed to the different device structures and to the different experimental conditions (e.g., the power and duration of the microwave excitation pulses).

VI. CONCLUSIONS

In summary, we have implemented and characterised noninvasive nongalvanic thermometers, sensing either the electronic temperature of a Fermi reservoir or the local bosonic temperature in a semiconductor quantum dot device. For the DQD thermometer, we could obtain a state-of-the-art noise-equivalent temperature of 3 $\mathrm{mK}/\sqrt{\mathrm{Hz}}$ and identify a path to even lower noise levels, well below 1 $\mathrm{mK}/\sqrt{\mathrm{Hz}}$. By synchronizing temperature acquisition to a periodic sequence of microwave bursts, we could increase the signal-to-noise ratio and probe temperature variations on a microsecond time scale. While this time-resolved QD thermometry is demonstrated in a silicon MOS device, it could be readily reproduced in any other semiconductor platform, such as Si-Ge-based heterostructures. Hence the present work opens up new experimental prospects for understanding heating effects in semiconductor quantum processors and for tackling the widely unexplored field of experimental quantum thermodynamics in nanoelectronic systems [33].

ACKNOWLEDGMENTS

This research has been supported by the European Union Horizon 2020 research and innovation program, under Grant Agreements No. 951852 ["Quantum Large Scale Integration in Silicon" (QLSI) project] and No. 810504 [European Research Council (ERC) project "3D Integration Technology for Silicon Spin Qubits" (QUCUBE)], by "Formation Quantique" (QuantForm)–UGA program Grant No. ANR-21-CMAQ-0003, France 2030, and by the LabEx LANEF Grant No. ANR-10-LABX-51-01.

[1] G. M. Noah, T. H. Swift, M. de Kruijf, A. Gomez-Saiz, J. J. L. Morton, and M. F. Gonzalez-Zalba, CMOS on-chip thermometry at deep cryogenic temperatures, Appl. Phys. Rev. **11**, 021414 (2024).

[2] B. Undseth, O. Pietx-Casas, E. Raymenants, M. Mehmandoost, M. T. Mądzik, S. G. Philips, S. L. de Snoo, D. J. Michalak, S. V. Amitonov, L. Tryputen, B. P. Wuetz, V. Fezzi, D. D. Esposti, A. Sammak, G. Scappucci, and L. M. Vandersypen, Hotter is easier: Unexpected temperature dependence of spin qubit frequencies, Phys. Rev. X **13**, 041015 (2023).

[3] W. I. L. Lawrie, M. Rimbach-Russ, F. v. van Riggelen, N. W. Hendrickx, S. L. de Snoo, A. Sammak, G. Scappucci, J. Helsen, and M. Veldhorst, Simultaneous single-qubit driving of semiconductor spin qubits at the fault-tolerant threshold, Nat. Commun. **14**, 3617 (2023).

[4] K. Takeda, J. Yoneda, T. Otsuka, T. Nakajima, M. R. Delbecq, G. Allison, Y. Hoshi, N. Usami, K. M. Itoh, S. Oda, T. Kodera, and S. Tarucha, Optimized electrical control of a Si/SiGe spin qubit in the presence of an induced frequency shift, npj Quantum Inf. **4**, 54 (2018).

[5] E. Kawakami, T. Jullien, P. Scarlino, D. R. Ward, D. E. Savage, M. G. Lagally, V. V. Dobrovitski, M. Friesen, S. N. Coppersmith, M. A. Eriksson, and L. M. K. Vandersypen, Gate fidelity and coherence of an electron spin in an Si/SiGe quantum dot with micromagnet, Proc. Nat. Acad. Sci. **113**, 11738 (2016).

[6] C. H. Yang, R. C. C. Leon, J. C. C. Hwang, A. Saraiva, T. Tanttu, W. Huang, J. Camirand Lemyre, K. W. Chan, K. Y. Tan, F. E. Hudson, K. M. Itoh, A. Morello, M. Pioro-Ladrière, A. Laucht, and A. S. Dzurak, Operation of a silicon quantum processor unit cell above one kelvin, Nature **580**, 350 (2020).

[7] L. C. Camenzind, S. Geyer, A. Fuhrer, R. J. Warburton, D. M. Zumbühl, and A. V. Kuhlmann, A hole spin qubit in a fin field-effect transistor above 4 kelvin, Nat. Electron. **5**, 178 (2022).

[8] S. Gasparinetti, K. L. Viisanen, O.-P. Saira, T. Faivre, M. Arzeo, M. Meschke, and J. P. Pekola, Fast electron thermometry for ultrasensitive calorimetric detection, Phys. Rev. Appl. **3**, 014007 (2015).

[9] E. Gümüş, D. Majidi, D. Nikolić, P. Raif, B. Karimi, J. T. Peltonen, E. Scheer, J. P. Pekola, H. Courtois, W. Belzig, and C. B. Winkelmann, Calorimetry of a phase slip in a Josephson junction, Nat. Phys. **19**, 196 (2023).

[10] F. Giazotto, T. T. Heikkilä, A. Luukanen, A. M. Savin, and J. P. Pekola, Opportunities for mesoscopics in thermometry and refrigeration: Physics and applications, Rev. Mod. Phys. **78**, 217 (2006).

[11] C. W. J. Beenakker, Theory of Coulomb-blockade oscillations in the conductance of a quantum dot, Phys. Rev. B **44**, 1646 (1991).

[12] D. Maradan, L. Casparis, T.-M. Liu, D. E. F. Biesinger, C. P. Scheller, D. M. Zumbühl, J. D. Zimmerman, and A. C. Gossard, GaAs quantum dot thermometry using direct transport and charge sensing, J. Low Temp. Phys. **175**, 784 (2014).

[13] G. Nicolí, P. Märki, B. A. Bräm, M. P. Röösli, S. Hennel, A. Hofmann, C. Reichl, W. Wegscheider, T. Ihn, and K. Ensslin, Quantum dot thermometry at ultra-low temperature in a dilution refrigerator with a 4He immersion cell, Rev. Sci. Instrum. **90**, 113901 (2019).

[14] P. Torresani, M. J. Martínez-Pérez, S. Gasparinetti, J. Renard, G. Biasiol, L. Sorba, F. Giazotto, and S. De Franceschi, Nongalvanic primary thermometry of a two-dimensional electron gas, Phys. Rev. B **88**, 245304 (2013).

[15] I. Ahmed, A. Chatterjee, S. Barraud, J. J. L. Morton, J. A. Haigh, and M. F. Gonzalez-Zalba, Primary thermometry of a single reservoir using cyclic electron tunneling to a quantum dot, Commun. Phys. **1**, 1 (2018).

[16] J. Chawner, S. Barraud, M. Gonzalez-Zalba, S. Holt, E. Laird, Y. A. Pashkin, and J. Prance, Nongalvanic calibration and operation of a quantum dot thermometer, Phys. Rev. Appl. **15**, 034044 (2021).

[17] See the Supplemental Material at http://link.aps.org/supplemental/10.1103/PhysRevApplied.21.064039 for more information about the resonator, the tuning of the dot lead and DQD configurations, the fitting protocol, the noise-equivalent temperature, the charge relaxation time, the filtering, and a schematic of the device with its thermal anchoring. The Supplemental Material also contains Refs. [34–37].

[18] F. Vigneau, F. Fedele, A. Chatterjee, D. Reilly, F. Kuemmeth, M. F. Gonzalez-Zalba, E. Laird, and N. Ares, Probing quantum devices with radio-frequency reflectometry, Appl. Phys. Rev. **10**, 021305 (2023).

[19] M. F. Gonzalez-Zalba, S. Barraud, A. J. Ferguson, and A. C. Betz, Probing the limits of gate-based charge sensing, Nat. Commun. **6**, 6084 (2015).

[20] M. G. House, T. Kobayashi, B. Weber, S. J. Hile, T. F. Watson, J. van der Heijden, S. Rogge, and M. Y. Simmons, Radio frequency measurements of tunnel couplings and singlet-triplet spin states in Si:P quantum dots, Nat. Commun. **6**, 8848 (2015).

[21] B. Bertrand, H. Flentje, S. Takada, M. Yamamoto, S. Tarucha, A. Ludwig, A. D. Wieck, C. Bäuerle, and T. Meunier, Quantum manipulation of two-electron spin states in isolated double quantum dots, Phys. Rev. Lett. **115**, 096801 (2015).

[22] H. G. J. Eenink, L. Petit, W. I. L. Lawrie, J. S. Clarke, L. M. K. Vandersypen, and M. Veldhorst, Tunable coupling and isolation of single electrons in silicon metal-oxide-semiconductor quantum dots, Nano Lett. **19**, 8653 (2019).

[23] J. I. Colless, A. C. Mahoney, J. M. Hornibrook, A. C. Doherty, H. Lu, A. C. Gossard, and D. J. Reilly, Dispersive readout of a few-electron double quantum dot with fast rf gate sensors, Phys. Rev. Lett. **110**, 046805 (2013).

[24] A. Blais, A. L. Grimsmo, S. Girvin, and A. Wallraff, Circuit quantum electrodynamics, Rev. Mod. Phys. **93**, 025005 (2021).

[25] K. D. Petersson, C. G. Smith, D. Anderson, P. Atkinson, G. A. C. Jones, and D. A. Ritchie, Charge and spin state readout of a double quantum dot coupled to a resonator, Nano Lett. **10**, 2789 (2010).

[26] N. C. van der Vaart, S. F. Godijn, Y. V. Nazarov, C. J. P. M. Harmans, J. E. Mooij, L. W. Molenkamp, and C. T. Foxon, Resonant tunneling through two discrete energy states, Phys. Rev. Lett. **74**, 4702 (1995).

[27] R. J. Zieve, D. E. Prober, and R. G. Wheeler, Low-temperature electron-phonon interaction in Si MOSFETs, Phys. Rev. B **57**, 2443 (1998).

[28] S. Gasparinetti, F. Deon, G. Biasiol, L. Sorba, F. Beltram, and F. Giazotto, Probing the local temperature of a two-dimensional electron gas microdomain with a quantum dot: Measurement of electron-phonon interaction, Phys. Rev. B **83**, 201306 (2011).

[29] T. H. Stoof and Y. V. Nazarov, Time-dependent resonant tunneling via two discrete states, Phys. Rev. B **53**, 1050 (1996).

[30] E. Dupont-Ferrier, B. Roche, B. Voisin, X. Jehl, R. Wacquez, M. Vinet, M. Sanquer, and S. De Franceschi, Coherent coupling of two dopants in a silicon nanowire probed by Landau-Zener-Stückelberg interferometry, Phys. Rev. Lett. **110**, 136802 (2013).

[31] M. Urdampilleta, A. Chatterjee, C. C. Lo, T. Kobayashi, J. Mansir, S. Barraud, A. C. Betz, S. Rogge, M. F. Gonzalez-Zalba, and J. J. Morton, Charge dynamics and spin blockade in a hybrid double quantum dot in silicon, Phys. Rev. X **5**, 031024 (2015).

[32] S. G. J. Philips, M. T. Madzik, S. V. Amitonov, S. L. de Snoo, M. Russ, N. Kalhor, C. Volk, W. I. L. Lawrie, D. Brousse, L. Tryputen, B. P. Wuetz, A. Sammak, M. Veldhorst, G. Scappucci, and L. M. K. Vandersypen, Universal control of a six-qubit quantum processor in silicon, Nature **609**, 919 (2022).

[33] J. P. Pekola, Towards quantum thermodynamics in electronic circuits, Nat. Phys. **11**, 118 (2015).

[34] Z. Penfold-Fitch, F. Sfigakis, and M. Buitelaar, Microwave spectroscopy of a carbon nanotube charge qubit, Phys. Rev. Appl. **7**, 054017 (2017).

[35] R. Mizuta, R. M. Otxoa, A. C. Betz, and M. F. Gonzalez-Zalba, Quantum and tunneling capacitance in charge and spin qubits, Phys. Rev. B **95**, 045414 (2017).

[36] P. Welch, The use of fast Fourier transform for the estimation of power spectra: A method based on time averaging over short, modified periodograms, IEEE Trans. Audio. Electroacoustics **15**, 70 (1967).

[37] J. R. Petta, A. C. Johnson, C. M. Marcus, M. P. Hanson, and A. C. Gossard, Manipulation of a single charge in a double quantum dot, Phys. Rev. Lett. **93**, 186802 (2004).